Journal of Building Engineering 83 (2024) 108432

Contents lists available at ScienceDirect

Journal of Building Engineering

journal homepage: www.elsevier.com/locate/jobe

Improvement of axial deformation prediction in high-rise buildings with filed monitoring and adaptive unscented Kalman filter

Yun Zhou [a], Xianming Luo [b,*], Wenjie Zhang [b], Peng Ye [b], Jiahao Chen [b], Zong Du [c]

[a] Key Laboratory for Damage Diagnosis of Engineering Structures of Hunan Province, Key Laboratory of Building Safety and Energy Efficiency of the Ministry of Education, College of Civil Engineering, Hunan University, Changsha, 410082, China
[b] College of Civil Engineering, Hunan University, Changsha, 410082, China
[c] Senior Engineer, China Construction Third Bureau First Engineering Co., Ltd, Wuhan, 430040, China

ARTICLE INFO

Keywords:
Axial deformation
High-rise building
Vertical members
Structural strain monitoring
Kalman filter
Concrete creep and shrinkage

ABSTRACT

The deformation of vertical reinforced concrete members in high-rise buildings during their construction is constantly changing due to the complexity of the deformation mechanism, as well as the uncertainties that arise during the construction process; in some cases, accurate estimation of the vertical displacement is crucial. Based on on-site strain monitoring data and an adaptive unscented Kalman filter, this paper establishes a state equation for the axial deformation process. The elastic, inelastic and temperature deformation of concrete during the entire construction process are reasonably considered. Deformation is predicted using both the traditional Kalman filter and unscented Kalman filter, both of which achieved satisfactory results. But the unscented Kalman filter can improve the prediction accuracy and robustness by utilizing unscented transformations. Anomaly detection is integrated into every inference step to detect abrupt changes in external conditions and dynamically adjust calculation parameters, thereby reducing the dependency of the prediction results on input parameters.

1. Introduction

As the construction industry continues to innovate and push boundaries, high-rise buildings are being designed and built to ever-greater heights, setting new records with each successive project. Accurate prediction of the axial deformation of vertical members in high-rise structures is imperative since excessive axial deformation can lead to abnormal elevator operation, pipeline damage, local cracking, and irregularities. Furthermore, the differences in axial deformation among twin-towers can cause the connection support system to tilt and deviate from their original position, resulting in additional shear forces and bending moments [1–3]. Axial deformation is mainly caused by the concrete properties, which is related to elastic, creep, and shrinkage deformation. In addition, due to the inconsistent gravity loads in the construction process, the elastic and creep deformation of member contains time-variant characteristics. The time-dependent behavior of concrete materials often leads to additional deformations that cannot be adequately considered during the design stage, particularly in high-rise structures which have long construction periods and exceptional structural heights [4,5]. Regarding the concrete creep and shrinkage, different codes and standards have related provisions, such as MC 2010 [6]

* Corresponding author.
E-mail addresses: zhouyun05@hnu.edu.cn (Y. Zhou), luoxianming@hnu.edu.cn (X. Luo), zhangwj29@hnu.edu.cn (W. Zhang), ye0607@hnu.edu.cn (P. Ye), cjiahao@hnu.edu.cn (J. Chen), carzy_2727@qq.com (Z. Du).

https://doi.org/10.1016/j.jobe.2023.108432
Received 6 June 2023; Received in revised form 24 November 2023; Accepted 31 December 2023
Available online 1 January 2024

and ACI 209R-92 [7]. In addition, there are specialized computational models proposed by some scholars, such as the B3 model [8] and the GL2000 model [9]. During the construction phase, the vertical members are subjected to intricate loading conditions, thereby rendering the appropriate calculation for additional deformation during the construction process a crucial engineering concern.

Axial deformation in high-rise buildings has been extensively studied. Fintel et al. [10,11] conducted early research on the axial deformation of columns and compensation methods in high-rise structures, considering both elastic and inelastic deformation of the column during the construction phase. In the 1970s, the American Concrete Institute (ACI) organized a systematic structural monitoring study on the long-term axial deformation of three supertall buildings and verified the feasibility of predicting the time-dependent deformation of concrete columns based on the fundamental models of concrete shrinkage and creep [12–15]. Baker et al. [16] investigated the axial deformation of vertical members of the Burj Khalifa building caused by concrete shrinkage and creep, and the effectiveness of existing models and methods were validated in predicting the vertical deformation of supertall structures during the design and construction phases. Zou et al. [17] conducted a one-year shrinkage and creep test on a RC shear wall and found that the axial deformation of RC shear walls is underestimated by various codes and computational models. Wang et al. [18] predicted the axial deformation of vertical members considering the effect of humidity and found that the traditional B3 model overestimated the axial deformation of giant vertical members without considering humidity distribution. Gao et al. [4] predicted the strain of a vertical member in a 335 m supertall structure located in Wuhan by recording on-site strain data using the MC 2010 model found that the MC 2010 model underestimated the concrete deformation. Zhao et al. [19] proposed a prediction method for evaluating section strains of giant members by combining the B3 model and the fiber model and validated it in a supertall structure. They found that the predicted axial deformation of shear walls agreed well with the measured data, but there was a significant difference between the predicted and measured values for giant columns. Tahmasebinia et al. [20] analyzed the axial deformation of the Sydney Opera House due to concrete shrinkage and creep, and found that the maximum vertical deformation at the top of the structure caused by shrinkage and creep could reach 57.48 mm. Xia et al. [21] measured high-strength and low-shrinkage concrete strain changes in the components of the Canton Tower in China and found that the concrete shrinkage strain was only about 50 % of the predicted result by ACI 209 specification, and the creep strain was only about 40 % of the predicted strain according to the code formula. Blanc et al. [22] considered the complex axial deformation of vertical members caused by creep during the construction process and directly fitted polynomials and calibrated coefficients to the vertical deformation. Moragaspitiya et al. [3,23] proposed an analytical method to update the axial deformation of vertical members by establishing a certain relationship between the structural vibration characteristics and the axial deformation, and designed a finite element interlayer element to calculate the vertical deformation caused by construction load changes. Fan et al. [24] analyzed the axial deformation during the construction stage of three super high-rise buildings in China, and a pre-deformation compensation method was proposed to reduce the influence of axial deformation.

The above studies reveal the inconsistency that lie in the application of existing models for concrete time-dependent properties and the actual structures. Therefore, some scholars have attempted to update predictions of axial deformation using measured data. Li et al. [25] simulated the shrinkage and creep in RC structures under random loads using a BP model and simplified the time-variant reliability problem as a time-invariant one for prediction. Bazant et al. [26] creatively used the Bayesian inference method to predict the shrinkage and creep of concrete and updated the prediction results based on existing experimental data. Yang [27,28] also used early measurement data based on the Bayesian inference theory to reduce the uncertainty of concrete deformation, and evaluated the importance of input parameters. Jin et al. [29] proposed a prediction method which introduced various creep models and combined them by optimizing weights to long-term creep behavior.

The Kalman filter was introduced by Rudolf E. Kalman in 1960 as a solution to the problem of estimating the state of a linear dynamic system in the presence of uncertain and noisy measurements. Since then, it has become a widely used algorithm for estimation and control problems. Over time, the Kalman filter has given rise to address limitations or extend its applicability to specific scenarios. The Extended Kalman Filter (EKF) [30,31] and the Unscented Kalman Filter (UKF) [32,33] represent two prominent variants specifically designed to address the presence of nonlinear system models within the Kalman filter framework. These variants mitigate the impact of nonlinearity by approximating the nonlinear models with linear counterparts, thereby enabling the utilization of standard Kalman filter techniques. The Generalized Kalman Filter (GKF) [34] further extends the KF to include non-Gaussian measurement noise. The Particle Filtering-based Kalman Filter (PFKF) [35] combines the Kalman filter with particle filtering to address nonlinearity and non-Gaussian distributions. Kalman filtering has numerous technological applications. A common application is for guidance, navigation, and control of vehicles, particularly aircraft, spacecraft, and ship positioning dynamically. Moreover, Kalman filtering represents a widely employed concept within the realm of time series analysis, primarily utilized in domains including signal processing [36]. In civil engineering, the Kalman filter serves as a fundamental tool for state estimation and prediction in structural health monitoring (SHM). By assimilating sensor measurements with a dynamic model, it facilitates accurate assessment of structural behavior, including deformation, vibration, and damage detection [37–40]. This aids in identifying potential risks, ensuring the safety and integrity of civil infrastructure, and optimizing maintenance strategies. However, the application of Kalman filter estimation to civil structure monitoring, particularly in relation to axial compression-related deformation, is still relatively limited in research and practice [41].

Twin-tower high-rise buildings are a distinct architectural style that has attracted significant attention in academic discussions, feature two tall interconnected towers [42]. For connected twin-tower high-rise buildings, accurately estimating time-varying axial deformation is particularly crucial, especially when the heights of the towers differ. The corresponding floor elevation error of the connected position includes both the settlement difference and the axial deformation difference of the two towers, which would result in the inclination of the corridor in construction and a secondary internal force during the building operating state. To accurately predict the axial deformation of the vertical members, a system state equation is established and the calculation results and sensor data are integrated to predict and update axial deformation using an adaptive unscented Kalman filter.

2. Time-dependent properties of concrete

Time-dependent properties of concrete is commonly used in prediction models and codes including the MC 2010 model [6], ACI209R-92 model [7], B3 model [8], and GL2000 model [9]. The relative theoretical formulas and computing methods for different input variables can be found in Appendix A-D. The MC 2010 model was derived from the work of Muller et al. [43] and was calibrated based on laboratory tests on structural concretes. Engineers prefer this model over the ACI 209R-92 model, which is an empirical model developed by Branson and Christiason [44] with minor modifications introduced in ACI 209R. The accuracy of prediction using ACI 209R is limited, particularly when its simplest form is used. The GL2000 model [9] was made to conform to the ACI 209 model guidelines, except for the concrete compressive strength; the model only requires input data that is available to engineers at the beginning of the design. The B3 model proposes a mathematical description of over 10 physical phenomena affecting the creep and shrinkage, and uses the compliance function to reduce the risk of errors due to inaccurate values of the elastic modulus, while the other three models (MC 2010, ACI209R-92, and GL2000) used creep coefficients to characterize the ratio of the creep strain to elastic strain under the same stress rather than the compliance function. It is noteworthy that the strain predicted by the equation does not refer to the local strain at a specific point inside the component, but instead considers the global average strain related to the cross-section of the concrete element. This approach is advantageous in terms of its simplicity for engineers, but its drawback is that the calculated results are decoupled from the actual deformation phenomenon [45].

3. Time varying axial deformation model establishment

To accurately quantify axial deformations, it is necessary to not only measure the total deformation of the members, but also to identify the contributing factors that make up this deformation. By characterizing the composition of these various components, a more comprehensive understanding of the axial deformation of the vertical members can be obtained. This information can then be used to improve the design and construction processes, as well as to develop more effective strategies for monitoring and maintaining the structural integrity of the building over time.

During the construction process of the vertical members in high-rise structures, their axial deformation is composed of two parts [6,8,9]: one is stress-related deformation, which is caused by the gradual accumulation of self-weight of the upper structure (i.e. concrete creep and elastic deformation), the other is stress-independent deformation (i.e. shrinkage deformation and temperature deformation), as shown in Eq. (1).

$$\varepsilon(t) = \varepsilon_{c\sigma}(t) + \varepsilon_{cn}(t) \tag{1}$$

In the equation, $\varepsilon_{c\sigma}(t) = \varepsilon_e(t) + \varepsilon_c(t)$ represents stress-related strain, where $\varepsilon_e(t)$ is elastic strain and $\varepsilon_c(t)$ denotes creep strain of concrete. $\varepsilon_{cn}(t) = \varepsilon_{sh}(t) + \varepsilon_T(t)$ represents stress-independent strain, where $\varepsilon_{sh}(t)$ is shrinkage strain and $\varepsilon_T(t)$ is temperature strain.

When a high-rise building is under construction, the upper load is gradually increased with the increment of stories, and the overall dimension of the vertical members are gradually decreased in the height direction. Therefore, the axial load is constantly increasing over time. To facilitate the establishment of the deformation equation of the vertical members, where the deformation at a certain time (t) is only related to the previous time (t-1), the sampling frequency is set to one day, as shown in Fig. 1, then the strain can be represented as Eq. (2).

$$\varepsilon(t+1) = \varepsilon(t) + \Delta\varepsilon_T(t,t+1) + \Delta\varepsilon_{sh}(t,t+1) + \Delta\varepsilon_c(t,t+1) + \Delta\varepsilon_e(t,t+1) + w(t) \tag{2}$$

where $\Delta\varepsilon_T$, $\Delta\varepsilon_{sh}$, $\Delta\varepsilon_c$, $\Delta\varepsilon_e$ represents the temperature strain, shrinkage strain and elastic strain occurring during the time period from t-$(t+1)$ days, respectively, and $w(t)$ represents the theoretical error, which can be used to represent uncertainties during the construction process or load transfer. $\Delta\varepsilon_T$ can be obtained by multiplying the temperature change at time t-$(t+1)$ by the thermal expansion coefficient α_T; The shrinkage strain at any time $\varepsilon_{sh}(t)$ can be calculated using parameters of concrete and the formula in Appendix A.

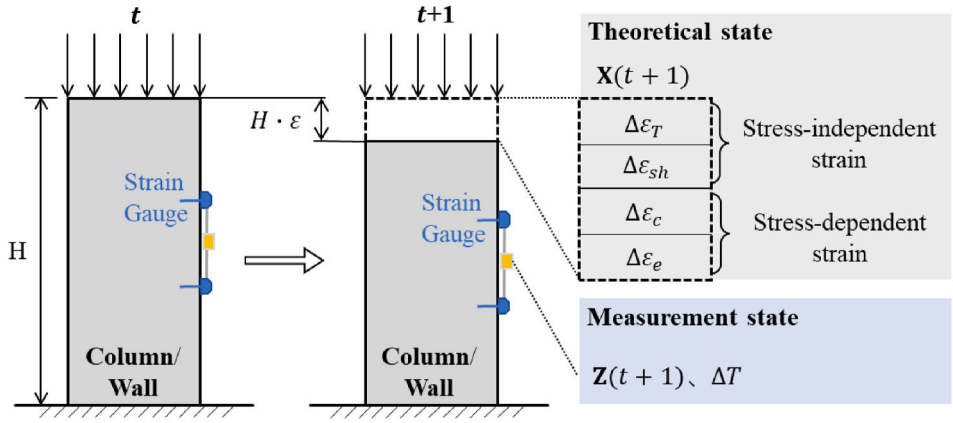

Fig. 1. Axial deformation composition and state schematic.

Subsequently, the increment shrinkage strain can be determined by subtracting the shrinkage strain at the previous time $\Delta\varepsilon_{sh}(t) = \varepsilon_{sh}(t) - \varepsilon_{sh}(t-1)$, $\Delta\varepsilon_c$ and $\Delta\varepsilon_e$ can be calculated using Eq. (3) and Eq. (4) [1].

$$\Delta\varepsilon_c = \frac{1}{E_{28}} \sum_{i=1}^{n} \varphi(t, t_i) \Delta\sigma(t, t_0) \tag{3}$$

$$\Delta\varepsilon_e = \left(\frac{\rho}{E_s} + \frac{1-\rho}{E_t}\right) \sum_{i=1}^{n} \Delta\sigma(t, t_i) \tag{4}$$

where E_{28} and E_t respectively represent the concrete elastic modulus at 28 days and a certain time of t; E_s is elastic modulus of rebar; φ is creep coefficient of concrete, which can be calculated using equations in Appendix A-D; ρ represents longitudinal reinforcement ratio; $\Delta\sigma$ represents the gravitational load changes, which is derived from a finite element model (the construction load is 2.5 kN/m^2); and n represents the number of floors (i.e. quantity of upper loads) at certain time t.

The state equation can be expressed as Eq. (5) by combining the four types of strain mentioned above into a state vector $\boldsymbol{X}$.

$$\boldsymbol{X}(t+1) = \boldsymbol{A} \cdot \boldsymbol{X}(t) + \boldsymbol{B}(t) \cdot \boldsymbol{U}(t) + \boldsymbol{w}(t) \tag{5}$$

where $\boldsymbol{X}(t) = [\varepsilon_T(t) \quad \varepsilon_{sh}(t) \quad \varepsilon_c(t) \quad \varepsilon_e(t)]^{\mathrm{T}}$; $\boldsymbol{A}$ represents the state transition matrix describing the relationship between the previous and current state, which is a 4 × 4 diagonal matrix($diag(1,1,1,1)$) in this paper; $\boldsymbol{B}$ is the input control matrix representing the relationship between the input vector and the state vector, and $\boldsymbol{U}$ is the input vector, which contains strain change during the time period from t-(t + 1), as shown in Eqs. (6) and (7). The residual error $\boldsymbol{w}(t)$ can be modeled by zero-mean Gaussian noise.

$$\boldsymbol{B}(t) = \begin{bmatrix} \alpha_T & 0 & 0 & 0 \\ 0 & 1 & 0 & 0 \\ 0 & 0 & \dfrac{1}{E_{28}} & 0 \\ 0 & 0 & 0 & \left(\dfrac{\rho}{E_s} + \dfrac{1-\rho}{E_t}\right) \end{bmatrix} \tag{6}$$

$$\boldsymbol{U}(t) = \begin{bmatrix} \Delta T(t, t+1) \\ \Delta\varepsilon_{sh}(t, t+1) \\ \sum_{i=1}^{n} \varphi(t, t_i) \Delta\sigma(t, t_0) \\ \sum_{i=1}^{n} \Delta\sigma(t, t_i) \end{bmatrix} \tag{7}$$

Eq. (6) and Eq. (7) can be used to represent the recursive relationship between the different strain states at each time step, where α_T is the coefficient of thermal expansion for concrete. Therefore, the strain state at each subsequent stage can be obtained by recursively calculating from an initial strain state. Furthermore, the sensors in the vertical members can only collect the overall strain each time, therefore the measurement equation can be represented as Eq. (8).

$$Z(t+1) = \boldsymbol{H} \cdot \boldsymbol{X}(t+1) + v(t+1) \tag{8}$$

where Z represents the measurement state, $\boldsymbol{H} = [1 \quad 1 \quad 1 \quad 1]$ is the measurement matrix, and v is the measurement noise, which can also be modeled by zero-mean Gaussian noise.

4. Robust adaptive unscented Kalman filter

4.1. Kalman filter

The Kalman filter is a recursive mathematical algorithm that uses a series of measurements observed over time, containing statistical noise and other inaccuracies. It operates on a predict-update cycle, where the predicted state estimate is calculated based on the system model and the current control input states. This process results in an improved estimate of the system state with each iteration.

The strain state system is established based on Eq. (5), the recursive prediction and update can be performed using the basic prediction and update equations of the Kalman filter after inputting initial strain state as shown by Eqs. (9)–(11).

Predictive equation:

$$\begin{cases} \widehat{\boldsymbol{X}}_t^- = \boldsymbol{A}\widehat{\boldsymbol{X}}_{t-1}^- + \boldsymbol{B}_{t-1}\boldsymbol{U}_{t-1} \\ \boldsymbol{P}_t^- = \boldsymbol{A}\boldsymbol{P}_{t-1}\boldsymbol{A}^{\mathrm{T}} + \boldsymbol{Q} \end{cases} \tag{9}$$

Kalman gain matrix:

$$K_t = \boldsymbol{P}_t^- \boldsymbol{H}^{\mathrm{T}} \left(\boldsymbol{H}\boldsymbol{P}_t^- \boldsymbol{H}^{\mathrm{T}} + R\right)^{-1} \tag{10}$$

Prediction update:

$$\begin{cases} \widehat{\boldsymbol{X}}_t = \widehat{\boldsymbol{X}}_t^- + K_t\left(Z_k - \boldsymbol{H}\widehat{\boldsymbol{X}}_t^-\right) \\ \overline{\boldsymbol{P}}_t = (\boldsymbol{I} - K_t\boldsymbol{H})\boldsymbol{P}_t^- \end{cases} \tag{11}$$

where the subscript t represents the time (in days); K_t represents the Kalman gain, which is a critical factor in the performance of the Kalman filter; $\boldsymbol{Q}$ represents the covariance matrix of the process noise in the state equation; R represents the covariance matrix of the measurement noise in the observation equation, and $\widehat{\boldsymbol{X}}_t^-$、 $\widehat{\boldsymbol{X}}_t$ represent the uncorrected strain state and the updated optimal state, respectively, It is evident that for the deformation equation, the initial strain state $\boldsymbol{X}(0) = [0 \quad 0 \quad 0 \quad 0]^{\mathrm{T}}$.

Considering the complexity of construction conditions, the prediction results of the Kalman filter algorithm are to some extent dependent on the initial covariance settings and the assumptions, in which the errors are simply modeled as zero-mean Gaussian noise. To reduce the errors resulting from these assumptions and improve the robustness of the deformation system, a Robust Adaptive Unscented Kalman Filter (RAUKF) method was adopted to improve the prediction accuracy.

4.2. Unscented Kalman filter (UKF)

The Unscented Kalman Filter (UKF) is a variation of the Kalman Filter that employs the Unscented Transformation (UT) to estimate the probability distribution of state variables. The UT utilizes a numerical integration approach known as the sampling points method. The UT approximates the Gaussian distribution by selecting a set of sampling points called sigma points. These sigma points are chosen to capture the mean and covariance of the Gaussian distribution and are propagated to estimate the state and measurement updates. The UKF iteratively updates the state estimate and covariance matrix, gradually improving the estimation of the system state and is known for its fast convergence. The flowchart and corresponding equations for the UKF are shown in Fig. 2. The calculation process can be divided into 5 steps. Step 1 is to set the initial state vector $\boldsymbol{X}_0$ and the estimated covariance matrix $\boldsymbol{P}_0$, which are usually based on prior knowledge or experience, and are key input parameters in the calculation. Reasonable initial values and errors of the state have a significant impact on the calculation accuracy. Step 2 is to construct the sigma point set, generally, there are $2n+1$ sigma points, where n is the dimension of the state vector, in this paper 9 sigma points are generated in each prediction step using Cholesky decomposition method. In Fig. 2, $\lambda = \xi^2(n+\kappa) - \eta$ is the scaling factor, $\xi = 0.01$ is the range of sigma points. $\kappa = 0$ is usually used, and $\eta = 2$ for Gaussian random variables. Step 3 is to calculate the predicted mean and corresponding covariance matrix for each point and combine these points with the weight factor. Step 4 is to calculate the corresponding observation matrix and Kalman gain coefficient; Step 5 is that the predicted state vector and covariance matrix are updated using the calculated Kalman gain, which is repeated for the next step,

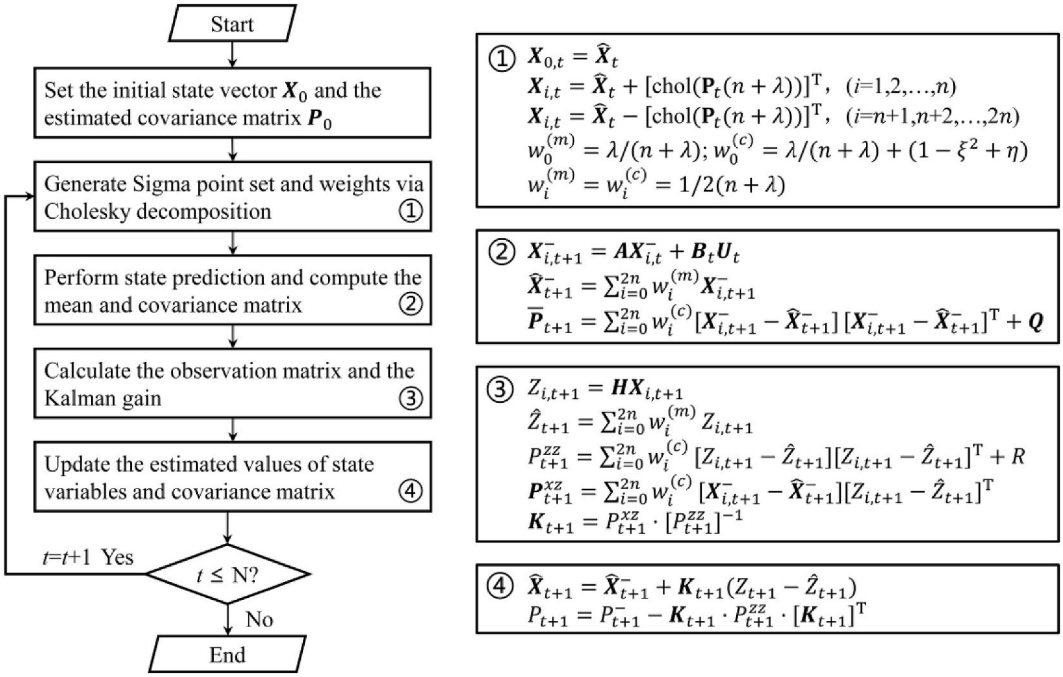

Fig. 2. Flowchart and calculating equations of UKF.

and the state obtained in the current step is used as the initial value for the next step, and so on, until the prediction process is completed.

Because UKF relies on the prior knowledge of the system and assumes that the system parameters remain constant throughout the process, prediction adjustments for environment changes are necessary for such things as severe weather conditions, seismic effects, and construction and dismantling of temporary platforms.

The UKF prediction requires manual specification of the initial values for process noise covariance $\boldsymbol{Q}$ and measurement noise covariance R, which directly affects the performance of the prediction. Trial-and-error is used to determine the appropriate value, which depends largely on the user's experience. And UKF may not converge and give inaccurate estimation results when inappropriate covariances are given [46].

4.3. Robust Adaptive Unscented Kalman Filter (RAUKF)

To address this issue, a Robust Adaptive Unscented Kalman Filter (RAUKF) is proposed to predict the strain state of vertical members, perform anomaly detection, and automatically adjust error covariance for system improvement. Firstly, a system anomaly detection process needs to be incorporated in each recursive step, as shown in Eq. (12) [47].

$$\delta_t = e_t^{\mathrm{T}} \left[P_t^{zz}\right]^{-1} e_t \tag{12}$$

Herein, $e_t = Z_t - \widehat{Z}_t$ is the prediction error and the calculation result of δ_t follows a chi-squared (χ^2) distribution. Through trial computations and to obtain better results, $\delta_{t,L} = 10$ was used in this study as the detection threshold for system anomalies (The selection of this threshold can be determined based on the degree of fluctuation observed in the measured data). If $\delta_t > \delta_{t,L}$, indicating the presence of anomaly in the system, adjustments to $\boldsymbol{Q}$ and R are required as shown in Eqs. (13)–(17) [48]. The threshold can be adjusted based on experience or existing data in specific practical situations.

$$\boldsymbol{Q}_t = (1-\lambda)\boldsymbol{Q}_t + \lambda\left(\boldsymbol{K}_t e_t e_t^{\mathrm{T}} \boldsymbol{K}_t^{\mathrm{T}}\right) \tag{13}$$

$$R_t = (1-\omega)R_t + \omega\left(e_t e_t^{\mathrm{T}} + \widehat{S}_t^{zz}\right) \tag{14}$$

$$\widehat{S}_t^{zz} = \sum_{i=0}^{2n} w_i^{(c)} [\boldsymbol{H}\cdot\widehat{\boldsymbol{X}}_t - Z_t]\cdot[\boldsymbol{H}\cdot\widehat{\boldsymbol{X}}_t - Z_t]^{\mathrm{T}} \tag{15}$$

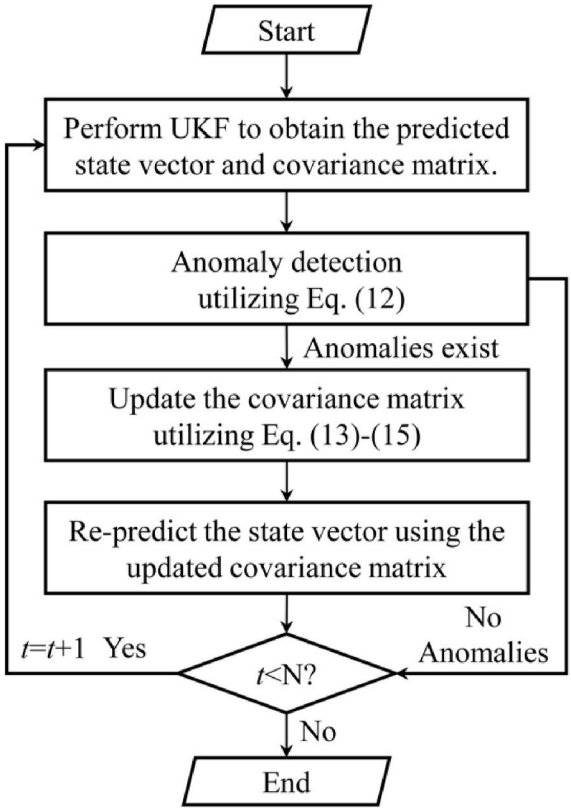

Fig. 3. Computation flowchart of RAUKF.

$$\lambda = max\left(\lambda_0, \left(\delta_t - a \cdot \delta_{t,L}\right)/\delta_t\right) \tag{16}$$

$$\omega = max\left(\omega_0, \left(\delta_t - b \cdot \delta_{t,L}\right)/\delta_t\right) \tag{17}$$

where ω_0 and λ_0 represents the lower limit of the weight coefficient and is set to 0.7 in this study. The tuning factor a and b is dependent on the actual environment, with a higher value of a or b, indicating a greater likelihood of using λ_0 or ω_0. Specially, how the trade-off between λ_0 and a will determine how sensitive the covariance update is to the new innovation statistics. In this study, the value of a and b have been set to 0.1.

After adjusting the two covariance matrices, the prediction can be updated, and the new covariance matrix can be utilized in the subsequent prediction process. The error in the prediction process can be adjusted in real-time while considering the impact of

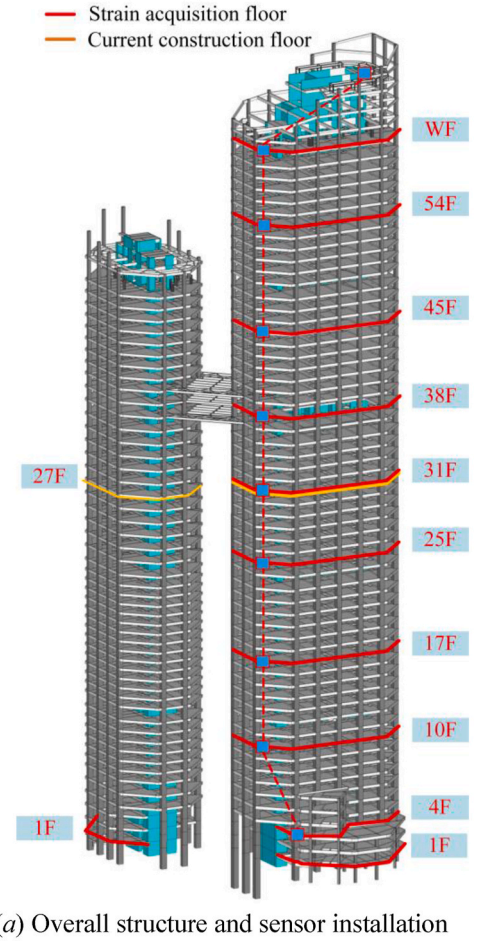

(*a*) Overall structure and sensor installation

(*b*) Project visualizations

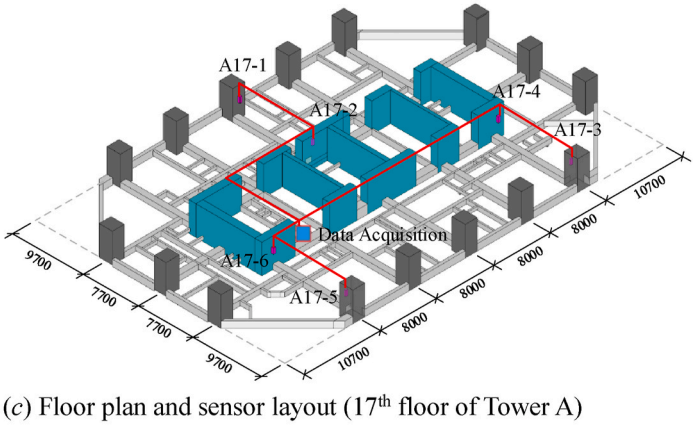

(*c*) Floor plan and sensor layout (17th floor of Tower A)

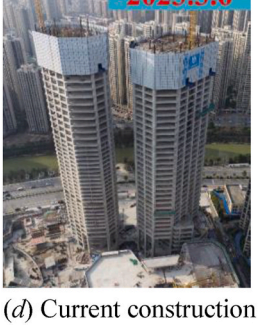

(*d*) Current construction progress

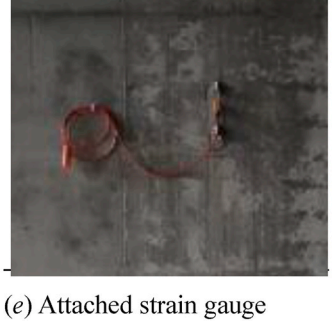

(*e*) Attached strain gauge

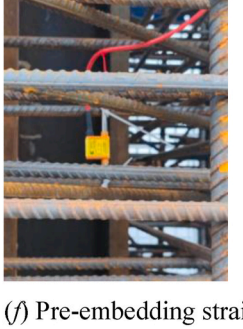

(*f*) Pre-embedding strain gauge

Fig. 4. Shengtong-meixihu international headquarters center.

environmental changes, thereby improving the robustness of the prediction process. The prediction process is shown in Fig. 3.

5. Case study: strain monitoring of a twin tower building

5.1. Overview of case study building

The case study building under-construction is a twin-tower connected high-rise building located in Changsha, Hunan Province, China, as shown in Fig. 4. This building occupies a site area of 27,000 m^2, including a three-story basement area of 72,000 m^2. The structure is composed of Tower A and Tower B, both of which were framed-core tube reinforced concrete (RC) structures connected by an aerial steel pedestrian bridge. Tower A is 59 stories above ground with a height of 279.65 m; Tower B has 49 stories above ground with a height of 219.65 m. The aerial steel pedestrian bridge is situated at an elevation of 150 m and is composed of steel truss girders and floor plates.

In general, the effect of concrete axial deformation during structural design is neglected, as are measures to compensate for vertical deformation during construction. Therefore, with the increment of axial deformation of concrete, the vertical displacement of each floor will accumulate making the structural elevation potentially inconsistent and connection of the two towers more difficult. Strain gauges are therefore installed on the vertical members of certain floors to monitor the strain data.

The structural health monitoring (SHM) system started in May 2022, which was after the first floor of Tower B was poured in April 2021 and first floor of Tower A was poured in September 2021. In total there were 64 strain sensors installed on Tower A, and 4 strain sensors on Tower B. The strain gauges were densely installed on Tower A as shown in Fig. 4(a). When the SHM system started to work, Tower A was constructed up to the 16th storey, therefore the attached strain gauges were installed on the vertical members below the 16th storey, while the pre-embedded strain gauges were installed above the 16th storey, as shown in Fig. 4(e)–(f). The layout of the sensors is shown in Fig. 4(c). Three sets of wall and column members were selected as SHM targets. The basic information of the vertical members and concrete materials is shown in Table 1.

5.2. Assumptions and results in computation

When evaluating the axial deformation of tall buildings, it is customary to employ certain assumptions to simplify the computational process and enhance efficiency, given the intricate nature of the structure and the non-linear behavior of materials. These assumptions encompass various aspects, including but not limited to the following:(a) Assuming material homogeneity, wherein its properties remain constant across the entire member; (b) Presuming uniform deformation in each member across all floors, thereby enabling the strain at any point on the member to represent the strain of the entire floor; (c) Assuming loads to be perpendicular to the axial direction and uniformly distributed throughout the entire structure; (d) Considering the structure to be in an elastic state during the construction stage, with solely vertical loads being considered for the calculation of axial deformation. These assumptions can significantly simplify the complex computation and enable engineers to determine the deformation and stability of the structure more efficiently, thereby facilitating the design and construction of high-rise buildings.

To confirm the variation in computation among various codes and to choose an appropriate theoretical model, a comparison was firstly made between the results obtained from equations in each model and the measured data, using the vertical components at the 17th floor of Tower A as an example, as shown in Fig. 5.

From Fig. 5, it can be observed that there are substantial differences in the predicted shrinkage, elasticity, and creep strain, which collectively constitute to deformation. For instance, according to the MC 2010 model [6], shrinkage deformation is dominant followed by elastic deformation, with creep deformation the smallest; the strain estimation by ACI 209R-92 [7] have similar regularity while the three components are more evenly distributed. On the other hand, the B3 model [8] is considered to have the largest proportion of creep deformation, followed by elastic deformation, and then shrinkage deformation. The GL2000 model [9] suggests that elastic deformation is the largest for the vertical components, followed by creep deformation and shrinkage deformation. However, the results of a study, which examined four different models, indicate that the magnitudes of shrinkage and creep deformations are comparable to that of elastic deformation, all falling within the same order of magnitude [49], so the concrete shrinkage and creep deformation need to be considered together with elastic deformation. The axial deformation of the vertical members can be obtained by multiplying the layer height by the strain.

When predicting the overall deformation of the columns (A17–1, A17-3), the MC 2010 [6] code presents the best prediction accuracy. However, when predicting the overall deformation of the shear walls (A17–2, A17-6), the final deformation values estimated by the GL 2000 [9] model was closer to the collected data, but there were large deviations from the measured results in the initial loading and intermediate loading stages, which was consistent with the experimental results of Zou et al. [49]. It is inferred that this

Table 1
Information of vertical members.

	A17-1	A17-2	A17-3	A17-4	A17-5	A17-6
Reinforcement ratio, %	0.95 %	0.91 %	0.95 %	0.91 %	0.95 %	0.91 %
Cross-sectional dimensions, mm	1900 × 1700	6800 × 1000	1900 × 1700	4850 × 1000	1900 × 1700	3750 × 1000
Nominal dimensions, mm	897.2	873	897.2	789.5	897.2	789.5

Height, mm	4100	Water content, kg/m^3	148	Aggregate content, kg/m^3	1760
f_c, MPa	60	Fine aggregate ratio, %	44	Slump of Concrete, mm	180
w/c	0.27	Cement type	P II 52.5	Cement content, kg/m^3	405

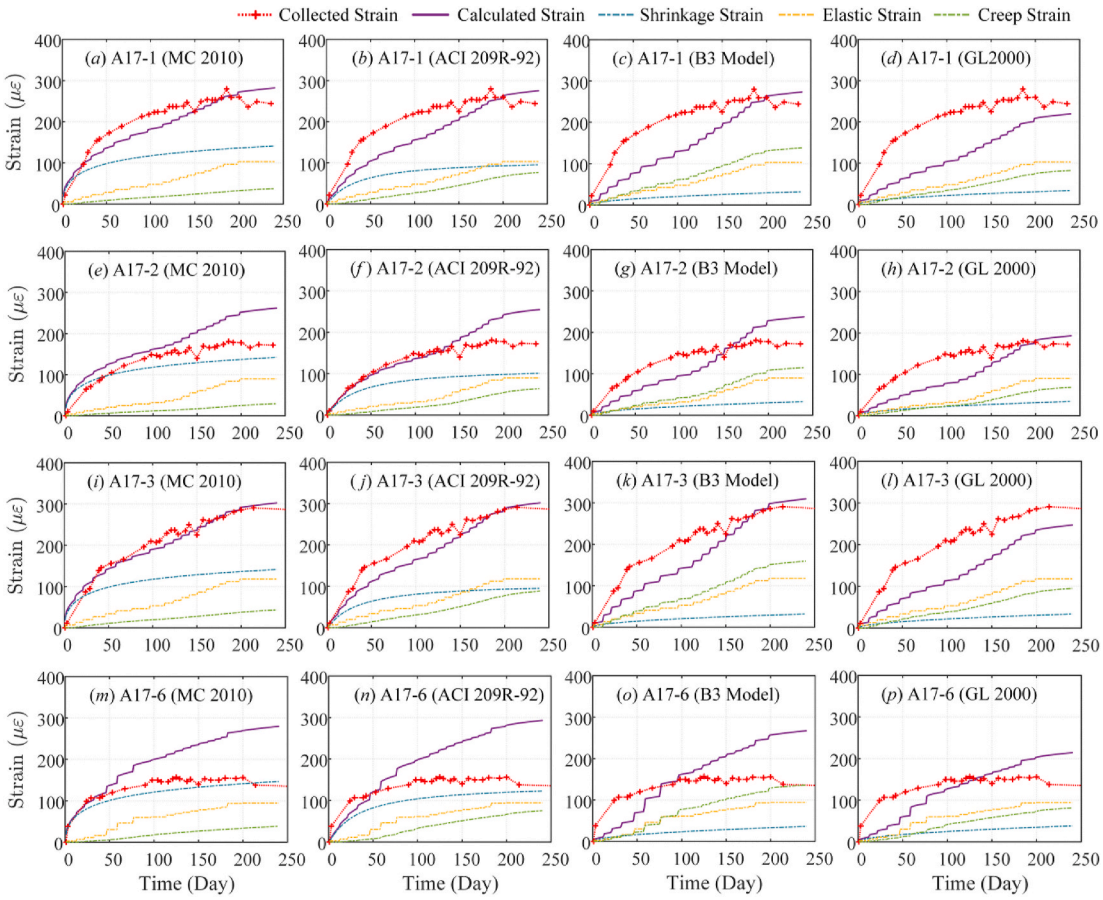

Fig. 5. Comparison between code computation results and measured data: (*a*)~(*d*): A17-1 column; (*e*)~(*h*): A17-2 shear wall; (*i*)~(*l*): A17-3 column; (*m*)~(*p*): A17-2 shear wall.

difference may be caused by the existing code and theoretical models through regression analyses of the experimental results in laboratory conditions. Furthermore, most of the tests were conducted under constant axial loads, environmental temperature and humidity [50,51,52]. But in actual engineering, the conditions are much more complicated, and the vertical members are constrained by the horizontal members.

It can be observed that the vertical deformation of the columns is larger than that of the shear walls. This is likely because the columns are subjected to a greater axial compression ratio. Furthermore, in this case, the frame columns are located at the outer edge of the structure and are more exposed to climate variations during the curing process when compared to the shear walls, resulting in less favorable curing conditions for the columns.

In practical engineering, the vertical members are significantly larger than laboratory specimens. Therefore, while some parameters may fall within the range of calculation equations specified in standards (Appendix E), there are additional factors that must be carefully considered during the design process. Fig. 6(*a*)(*b*) present a comparison between the volume-to-surface ratio (V/S) of the components and the number of V/S specimens in RILEM shrinkage and creep database [52,53,54], which contains roughly 1400 creep and 1800 shrinkage curves. The V/S ratio of most experimental specimens ranged from 0 to 50 mm, while the V/S ratio of vertical members in the 17th storey of Tower A was far beyond the range of the data in the database. On the other hand, the axial compression stress of laboratory specimens is usually controlled between 5 and 35 MPa (Fig. 6(*c*)), and the axial compression ratio is usually controlled between 0.2 and 0.5 (Fig. 6(*d*)). However, in actual structures, especially high-rise buildings, the cross-sectional dimensions of the vertical components, particularly those at the bottom, are often primarily dominated by horizontal loads, and the actual axial compression stress during the construction process does not exceed 10 MPa, and the axial compression ratio does not exceed 0.1. Fig. 6 (*c*)(*d*) show that the axial compression conditions of the components also deviate from the mean of the normal distribution in the database. Therefore, the use of theoretical models in code to predict the vertical deformation of high-rise structures is suspect, and therefore novel methods are required to more accurately update predicted trends and results.

To improve calculation accuracy, the methods outlined in sections 3 and 4 of this paper were used to predict the axial deformation over 250 days for vertical members in the 17th storey. Fig. 7 shows the vertical deformation predicted using traditional Kalman filter (the input vectors for the shrinkage and creep were calculated using MC 2010 model). Compared with the results in Fig. 5, the prediction accuracy was greatly improved, it can be observed that for different members, the Kalman filter can obtain ideal results after a

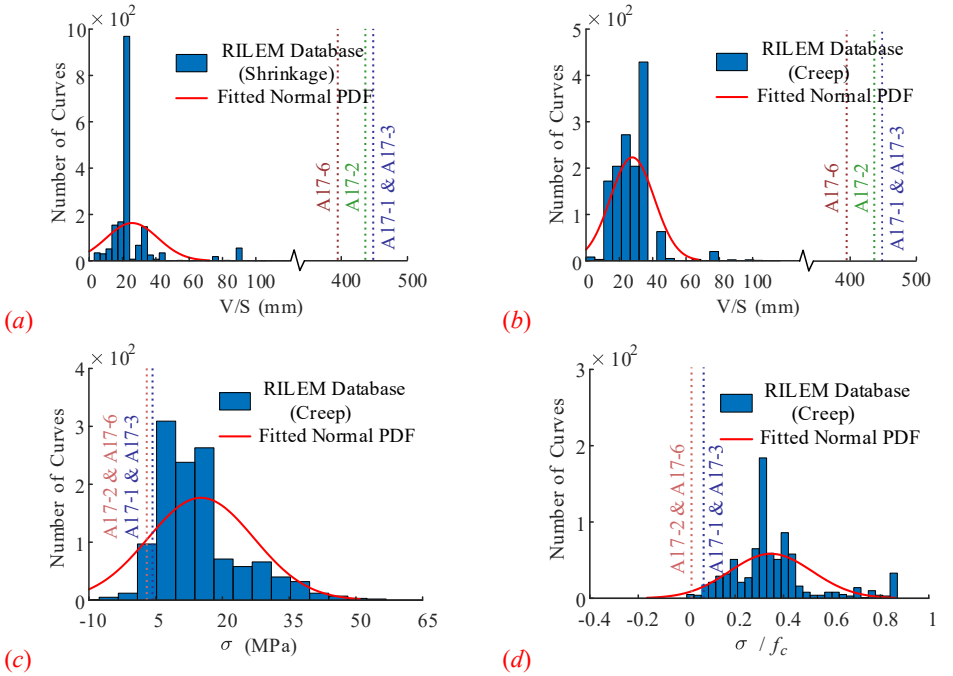

Fig. 6. Comparison of calculated vertical member parameters with database.

certain step of data fusion. The blue dashed line in Fig. 7 represents the change trend in the Kalman gain. It can be seen that after 40 days, the Kalman gain gradually converges, indicating that the predicted results and the system state equation of the deformation are reasonable and reliable.

To improve the prediction accuracy and the robustness of the prediction process, the axial deformation predicted results using UKF and RAUKF for the A17-1 component are given in Fig. 8(*a*)(*b*). It can be seen that UKF can further improve the prediction accuracy

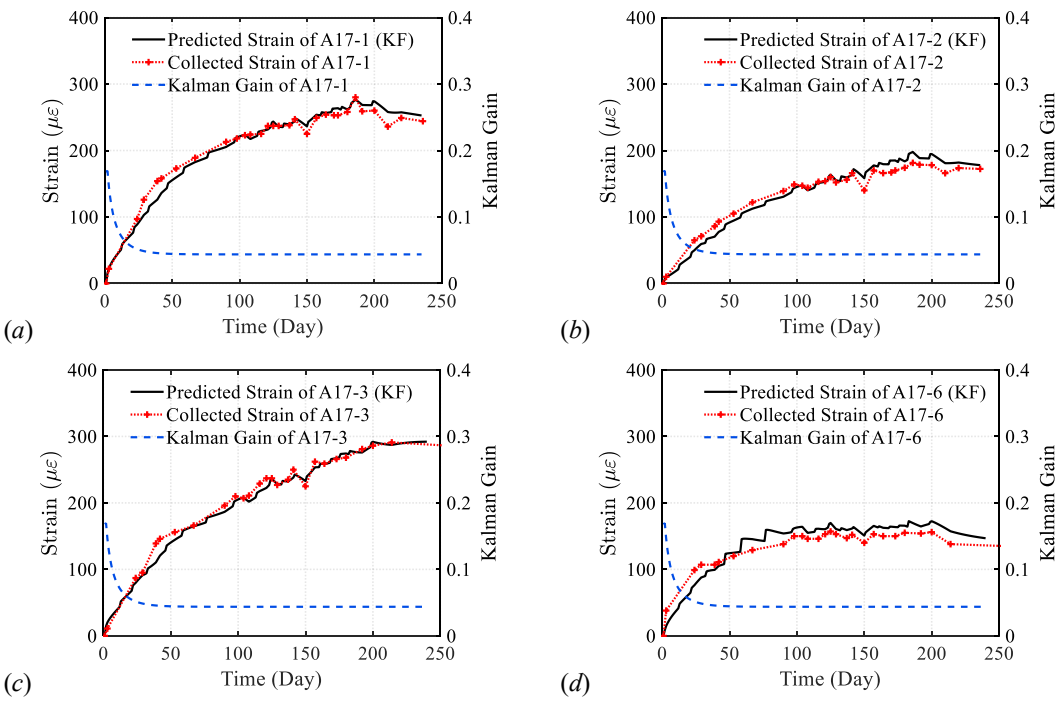

Fig. 7. Predicted results of traditional Kalman filter.

compared to traditional KF, while RAUKF is closer to the collected data. The innovative UKF and RAUKF results are shown in Fig. 8(*c*) where it is evident that RAUKF is much smaller than that of UKF. Furthermore, it is apparent that the utilization of RAUKF for anomaly detection yields error magnitudes that are generally confined within the predefined detection threshold ($\delta_{t,L} = 10$), which can be adjusted according to specific circumstances. Similar conclusions can be drawn from other vertical members in the 17th floor of Tower A, as shown in Fig. 8(*d*)~(*l*).

The proposed methodology can be employed for strain prediction or completion of missing strain data, thereby providing data support for vertical member compensation during construction [55]. The Kalman filter, based on the current system state equation, enables the prediction of any future state (Eq. (9)). As the Kalman filter updates the current state at each iteration (Eq. (10) and Eq. (11)), the system state gradually converges to the true value with an increasing number of iterations, manifested by the convergence of the Kalman gain coefficient. Therefore, when utilizing the Kalman filter for system state prediction, it is necessary to ensure a certain number of initial iterations. In this case, based on the convergence of the Kalman gain coefficients shown in Fig. 7, it is recommended to have a minimum of 30 days of initial iterative computations. Otherwise, the accuracy of the prediction results will heavily rely on the accuracy of the state equation. Moreover, the proposed RAUKF not only enhances system robustness but also enables anomaly detection and diagnosis. By comparing the predicted results with the actual measurements, deviations or anomalies can be identified. When deviations fall within the threshold range, automatic correction is applied, while deviations beyond the threshold range prompt either data exclusion or warning notifications.

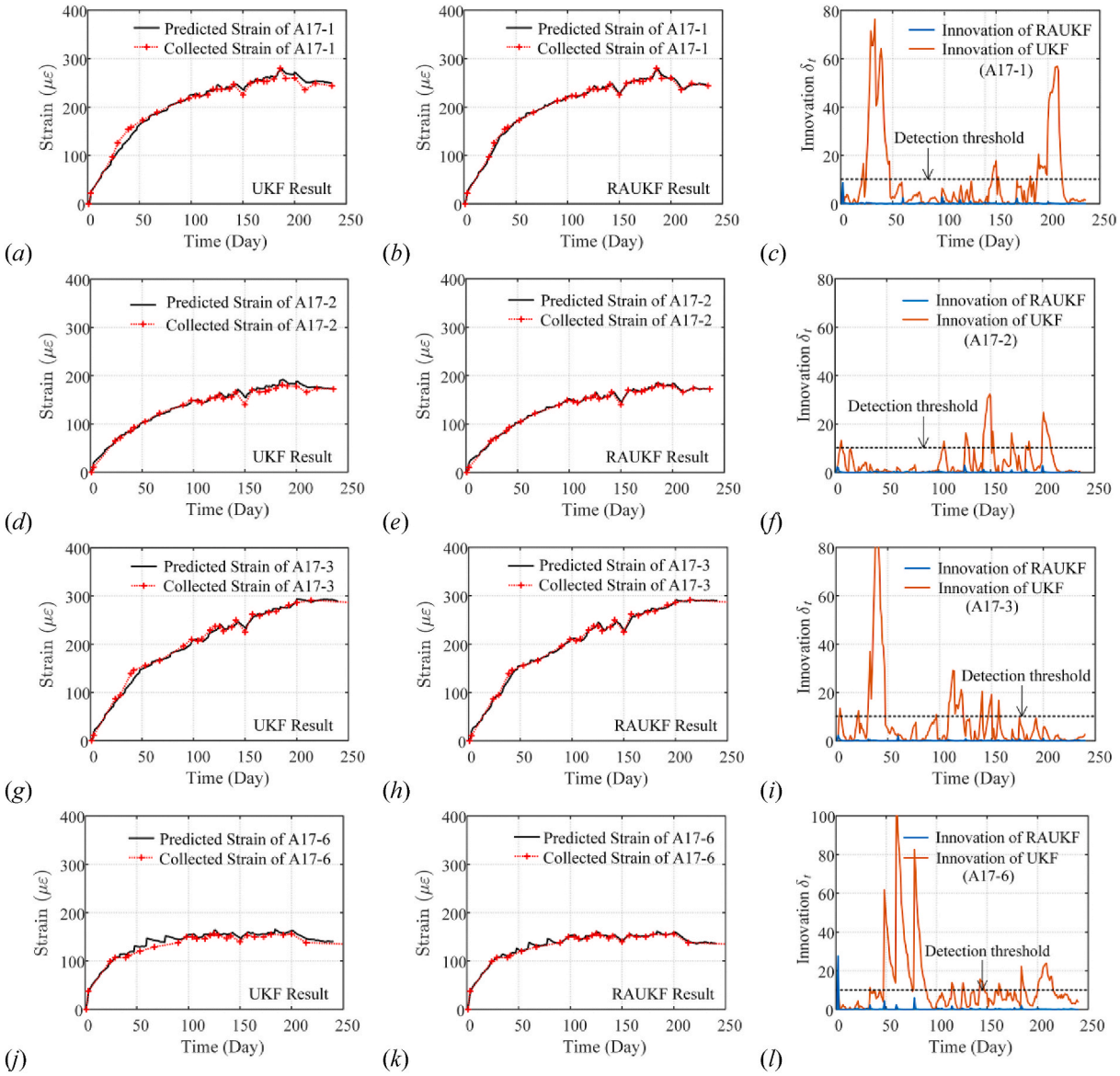

Fig. 8. Predicted results of UKF and RAUKF.

6. Conclusions

A prediction method for the axial deformation of vertical members in super high-rise structures based on an adaptive unscented Kalman filter was proposed. By establishing the system state equation for the entire process of axial deformation and incorporating the field monitoring strains of vertical members, the calculated results and measured data were fused to reduce prediction errors. The unscented transformation was then employed to further improve the prediction accuracy. Moreover, anomaly detection was incorporated into the inference process to adapt to various environmental mutations during construction and enhance the robustness of the deformation system.

1. A construction monitoring system was established in a super high-rise twin-tower composite structure. Axial deformation strain was monitored in vertical members throughout the construction process. The axial deformation was predicted and compared using four widely recognized codes and theoretical models. Results showed a large discrepancy compared to the actual measurement.
2. The system state equation for the axial deformation process of the vertical members was established, considering the effects of concrete shrinkage, creep, elasticity, and temperature deformation. The traditional Kalman filtering method was employed to recursively predict the deformation development. The results indicate that the Kalman filtering method could improve the prediction accuracy, and the gain in the Kalman filtering converged within a relatively short time, which compensated for errors in the theoretical models.
3. The robustness and prediction accuracy of the calculation results were improved by mapping the state equation to multiple sigma points through unscented transformation, and then recombining them using weight coefficients. The results showed that the unscented Kalman filter (UKF) could enhance the prediction of axial deformation compared to traditional Kalman filtering, without requiring a more complex calculation process.
4. Anomaly detection was incorporated in the prediction process, such as environmental mutations, sensor damage, and human-induced damage. Timely corrections were made for anomalies, and the covariance matrix in the inference process was adaptively adjusted using predicted innovation to reduce the influence of the initial input parameters on the predicted results.

CRediT authorship contribution statement

Yun Zhou: Writing – review & editing, Project administration, Conceptualization. **Xianming Luo:** Writing – original draft, Methodology, Investigation, Conceptualization. **Wenjie Zhang:** Validation, Data curation. **Peng Ye:** Validation, Data curation. **Jiahao Chen:** Validation, Data curation. **Zong Du:** Resources, Project administration, Funding acquisition.

Declaration of Competing interest

The authors declare that they have no conflict of interest.

Data availability

No data was used for the research described in the article.

Acknowledgements

The authors sincerely appreciate the funding support provided by the National Natural Science Foundation of China (NSFC) (No. 51878264, No. 52278306), the Science and Technology Progress and Innovation Project of the Department of Transportation of Hunan Province (201912), the Natural Science Foundation of Hunan Province of China (No. 2023JJ70003), and the Hydraulic Science and Technology Project of the Hunan Provincial Department of Water Resources (No. XSKJ2023059-31).

Appendix A

MC 2010

Concrete strength, MPa	$f_{cr}(t) = f_c \bullet \exp\left\{s_c \bullet \left[1 - \left(\frac{28}{t}\right)^{0.5}\right]\right\}$	Concrete elastic modulus, MPa	$E_c = 21.5 \bullet 10^3 \bullet \left(\frac{f_{cr}}{10}\right)^{1/3}$
Shrinkage	$\varepsilon_{sh}(t,t_c) = -\alpha_{bs}\left(\frac{0.1 \bullet f_c}{6 + 0.1 \bullet f_c}\right)^{2.5} \bullet 10^{-6} \bullet (1 - \exp(-0.2 \bullet \sqrt{t})) + \varepsilon_{cds0} \bullet \beta_{RH} \bullet \beta_{ds}$ $\varepsilon_{cds0} = [(220 + 110 \bullet \alpha_{ds1}) \bullet \exp(-\alpha_{ds2}) \bullet f_c] \bullet 10^{-6}$ $\beta_{RH} = \begin{cases} -1.55 \bullet [1 - (RH/100)^3] & 40 \le RH < 99\% \bullet (35/f_c)^{0.1} \\ 0.25 & RH > 99\% \bullet (35/f_c)^{0.1} \end{cases}$ $\beta_{ds} = \left(\frac{t - t_c}{0.035 \bullet h^2 + (t - t_c)}\right)^{0.5}$		

(*continued on next page*)

(*continued*)

Concrete strength, MPa	$f_{ct}(t) = f_c \bullet \exp\left\{s_c \bullet \left[1 - \left(\frac{28}{t}\right)^{0.5}\right]\right\}$	Concrete elastic modulus, MPa	$E_c = 21.5 \bullet 10^3 \bullet \left(\frac{f_{ct}}{10}\right)^{1/3}$
Creep	$\varphi(t,t_0) = \frac{1.8}{(f_c)^{0.7}} \bullet \ln\left(\left(\frac{30}{t_0} + 0.035\right)^2 \bullet (t - t_0) + 1\right) + \beta_{dc}(f_c) \bullet \beta(RH) \bullet \beta_{dc}(t_0) \bullet \beta_{dc}(t,t_0)$ $\beta_{dc}(f_c) = \frac{412}{(f_c)^{1.4}}; \beta(RH) = \frac{(1 - RH/100)}{\sqrt[3]{0.1 \bullet h/100}}; \beta_{dc}(t_0) = \frac{1}{0.1 + t_0^{0.2}};$ $\beta_{dc}(t,t_0) = \left(\frac{(t - t_0)}{\beta_h + (t - t_0)}\right)^{\gamma(t_0)}$		

Notes: f_c = compressive strength of concrete under normal curing conditions after 28 days; s_c、α_{bs}、α_{ds1}、α_{ds2} = coefficient for cement type; $h = 2A_c/u$, A_c = cross-sectional area, u = perimeter of the component in contact with the external environment; t_c = starting time when the component is exposed to air; t_0 = time when load is applied; $\beta_h = 1.5 \bullet h + 250 \bullet (35/f_c)^{0.5} \le 1500 \bullet (35/f_c)^{0.5}$; $\gamma(t_0) = 1/2.3 + 3.5/\sqrt{t_0}$。

Appendix B

ACI209R-92

Concrete strength, MPa	$f_{ct}(t) = f_c \bullet \left(\frac{t}{a + bt}\right)$	Concrete elastic modulus, MPa	$E_c = 0.043\rho_c^{1.5}\sqrt{f_{ct}}$
Shrinkage	$\varepsilon_{sh}(t,t_c) = \varepsilon_{shu} \bullet \left(\frac{t - t_c}{35 + (t - t_c)}\right)$ $\varepsilon_{shu} = 780\gamma_{sh} \bullet 10^{-6}$ $\gamma_{sh} = \gamma_{sh,tc} \bullet \gamma_{sh,RH} \bullet \gamma_{sh,vs} \bullet \gamma_{sh,s} \bullet \gamma_{sh,\psi} \bullet \gamma_{sh,c} \bullet \gamma_{sh,\alpha}$		
Creep	$\varphi(t,t_0) = \frac{(t - t_0)^{0.6}}{10 + (t - t_0)^{0.6}}\varphi_u$ $\varphi_u = 2.35 \bullet \gamma_c$ $\gamma_c = \gamma_{c,t0} \bullet \gamma_{c,RH} \bullet \gamma_{c,vs} \bullet \gamma_{c,s} \bullet \gamma_{c,\psi} \bullet \gamma_{c,\alpha}$		

Notes: a、b = curing condition and the coefficient for cement type, respectively; ρ_c = unit weight of concrete; $\gamma_{sh,tc} = 1.202 - 0.2337\log(t_c)$; $\gamma_{sh,RH}$ = humidity correction coefficient; $\gamma_{sh,vs} = 1.2\exp(-0.00472(V/S))$; V is the volume of the component and S denotes the surface area of the component; $\gamma_{sh,s} = 0.89 + 0.00161s$, s refers to the slump of the concrete; $\gamma_{sh,\psi}$ = fine aggregate correction factor; $\gamma_{sh,c}$ is the cement content correction factor $= 0.75 + 0.00061c$, c is the cement content; $\gamma_{sh,\alpha} = 0.95 + 0.008\alpha \ge 1$; α is the air content in cement; $\gamma_{c,t0} = 1.25t_0^{-0.118}$; $\gamma_{c,RH} = 1.27 - 0.0067RH$; $\gamma_{c,vs} = 2/3(1 + 1.13\exp(-0.0213(V/S)))$; $\gamma_{c,s} = 0.082 + 0.00264s$; $\gamma_{c,\psi} = 0.46 + 0.09\alpha \ge 1$.

Appendix C

B3 Model

Concrete elastic modulus, MPa	$E_c = 4734\sqrt{f_c}$	Elastic modulus-time relationship	$E_{ct}(t) = E_c\left(\frac{t}{4 + 0.85t}\right)^{\frac{1}{2}}$
Shrinkage	$\varepsilon_{sh}(t,t_c) = -\varepsilon_{shu} \bullet k_h \bullet S_s(t - t_c)$ $\varepsilon_{shu} = -\varepsilon_{su}\frac{E_{ct}(607)}{E_{ct}(t_c + \tau_{sh})}$ $\varepsilon_{su} = -\alpha_1\alpha_2[0.019w^{2.1}f_c^{-0.28} + 270] \bullet 10^{-6}$ $S_s(t - t_c) = \tanh\left(\frac{t - t_c}{\tau_{sh}}\right)^{\frac{1}{2}}$ $\tau_{sh} = 85000t_c^{-0.08}f_c^{-0.25}\left[2k_s\left(\frac{V}{S}\right)\right]^2$		
Creep	$J(t,t_0) = \frac{127}{\sqrt{f_c}} + C_0(t,t_0) + C_d(t,t_0,t_c)$ $C_0(t,t_0) = 185.4c^{0.5}f_c^{-0.9}Q(t,t_0) + 53.766\left(\frac{w}{c}\right)^4 c^{0.5}f_c^{-0.9} \bullet \ln[1 + (t - t_0)^{0.1}] + 20.3\left(\frac{a}{c}\right)^{-0.7}\ln\left(\frac{t}{t_0}\right)$ $Q(t,t_0) = (0.086t_0^{2/9} + 1.21t_0^{4/9}) \bullet \left[1 + \left(\frac{[0.086t_0^{2/9} + 1.21t_0^{4/9}]^{-1}}{t_0^{-0.5}\ln[1 + (t - t_0)^{0.1}]}\right)^{r(t_0)}\right]^{-1/r(t_0)}$ $C_d(t,t_0,t_c) = 7.57 \bullet 10^5 f_c^{-1}\lvert\varepsilon_{shu}\rvert^{-0.6}\sqrt{\exp(-8H(t)) - \exp(-8H(t_0))}$ $\varphi(t,t_0) = E_{ct}(t_0)J(t,t_0) - 1$		

Notes: k_h = humidity correction coefficient; $k_h = 1 - (RH/100)^3$ when $RH/100 \leq 0.98$, $k_h = -0.2$ when $RH/100 \leq 0.98$; α_1、α_2 are constants related to the cement type and curing condition; k_s is the shape of cross-section coefficient; $r(t_0) = 1.7t_0^{0.12} + 8$; w = water content; a = aggregate content; $t_0' = \max(t_0, t_c)$; $H(t) = [1 - (1 - RH/100)S_s(t)]$.

Appendix D

GL2000 Model

Concrete strength, MPa	$f_{ct}(t) = f_c \bullet \left(\frac{t^{3/4}}{a + bt^{3/4}}\right)$	Elastic modulus-time relationship	$E_{ct}(t) = 3500 + 4300\sqrt{f_{ct}}$
Shrinkage	$\varepsilon_{sh}(t,t_c) = \varepsilon_{shu} \bullet \beta(h) \bullet \beta(t - t_c)$ $\varepsilon_{shu} = 1000k\left(\frac{30}{f_c}\right)^{1/2} \times 10^{-6}$ $\beta(t - t_c) = \left[\frac{(t - t_c)}{(t - t_c) + 0.15(V/S)^2}\right]^{1/2}$		
Creep	$\varphi(t,t_0) = \Phi(t_c)\left[2\left(\frac{(t - t_0)^{0.3}}{(t - t_0)^{0.3} + 14}\right) + \left(\frac{7}{t_0}\right)^{0.5}\left(\frac{t - t_0}{t - t_0 + 7}\right)^{0.5} + 2.5(1 - 1.086(RH/100)^2)\left(\frac{t - t_0}{t - t_0 + 0.15(V/S)^2}\right)^{0.5}\right]$ $\Phi(t_c) = \left[1 - \left(\frac{t_0 - t_c}{t_0 - t_c + 0.15(V/S)^2}\right)^{0.5}\right]^{0.5}$		

Notes: $a = 1.0$, b = 0.92 for type III cement; k is cement type correction coefficient = 1.15 for type III cement; $\beta(h) = (1 - 1.18(RH/100)^4)$.

Appendix E

Parameter ranges of each model

Input variables	Prediction Model			
	MC 2010	ACI 209R-92	B3	GL2000
f_c, MPa	12 to 120	-	17 to 70	16 to 82
a/c	-	-	2.5 to 13.5	-
Cement content, kg/m^3	-	279 to 446	160 to 720	-
w/c	-	-	0.35 to 0.85	0.40 to 0.60
Relative humidity, %	40 to 100	40 to 100	40 to 100	20 to 100
t_c (Moist cured)	$\leq$ 14 days	$\geq$ 1 day	$\geq$ 1 day	$\geq$ 1 day
t_0	$\geq$ 1 days	$\geq$ 7 days	$t_0 \geq t_c$	$t_0 \geq t_c \geq$ 1 day

Note: Stress in creep cannot exceed 0.4 f_c.

References

[1] L.B. Pan, P.C. Liu, S.L. Bakoss, Long-term shortening of concrete columns in tall buildings, J. Struct. Eng. 119 (7) (1993) 2258–2262.
[2] M.T.R. Jayasinghe, W.M.V.P.K. Jayasena, Effects of axial shortening of columns on design and construction of tall reinforced concrete buildings, Pract. Period. Struct. Des. Construct. 9 (2) (2004) 70–78.
[3] M. Praveen, T. David, P. Nimal, T. Chan, A numerical method to quantify differential axial shortening in concrete buildings, Eng. Struct. 32 (2010) 2310–2317.
[4] F. Gao, H. Zhou, H. Liang, S. Weng, H. Zhu, Structural deformation monitoring and numerical simulation of a supertall building during construction stage, Eng. Struct. 209 (2020) 110033.
[5] M.M. Elnimeiri, M.R. Joglekar, Influence of column shortening in reinforced concrete and composite high-rise structures, ACI Journal (1989) 55–86. SP 117-4.
[6] Ceb-Fip, Fib Model Code for Concrete Structures 2010, International Federation for Structural Concrete (fib), 2010.
[7] ACI Committee 209, Prediction of Creep, Shrinkage, and Temperature Effects in Concrete Structures(209R-92), American Concrete Institute, 1992.
[8] Z.P. Bazant, W. P Murphy, Creep and shrinkage prediction model for analysis and design of concrete structures-model B3, Mater. Struct. 28 (1995) 357–365.
[9] N.J. Gardner, M.J. Lockman, Design provisions for drying shrinkage and creep of normal-strength concrete, ACI Mater. J. 98 (2) (2001) 159–167.
[10] M. Fintel, S.K. Ghosh, H. Iyengar, Column shortening in tall structures: prediction and compensation. Skokie, IL, Portland Cement Association, 1987.
[11] M. Fintel, F.R. Khan, Effects of column creep and shrinkage in tall structures-analysis for differential shortening of columns and field observation of structures, ACI Journal 66–83 (1969) 957–967.
[12] D.W. Pfeifer, D.D. Magur A, H.G. Russell, W.G. Corley, Time dependent deformations in a 70 story structure, ACI Journal (1971) 159–186. SP 27-7.
[13] H.W. Russell, Field Instrumentation of Concrete Structures, ASTM special technical publications, 1980, pp. 63–77.
[14] H.W. Russell, K.N. Shiu, Creep and Shrinkage Behavior of Tall Buildings and Long Span Bridges, Springer Netherlands, Dordrecht, 1982, pp. 293–303.
[15] Chicago Committee on High-Rise Building, High-strength concrete in Chicago high-rise buildings. Materials Task Force, 1977.
[16] W.F. Baker, D.S. Korista, L.C. Novak, J. Pawlikowski, B. Young, Creep and shrinkage and the design of supertall buildings—a case study: the Burj dubai tower, ACI Journal SP 246–8 (2007) 133–148.
[17] D. Zou, T. Liu, J. Teng, C. Du, B. Li, Influence of creep and drying shrinkage of reinforced concrete shear walls on the axial shortening of high-rise buildings, Construct. Build. Mater. 55 (2014) 46–56.

[18] L. Wang, X. Zhao, C. Yan, Time-dependent vertical shortening prediction for super-tall buildings by using a modified B3 model to consider moisture distribution, Eng. Struct. 209 (2020) 109994.
[19] X. Zhao, L. Wang, Vertical shortening prediction for super-tall buildings considering enclosure effect and coupling effect, Struct. Des. Tall Special Build. 29 (2) (2019).
[20] F. Tahmasebinia, D. Fogerty, L.O. Wu, Z. Li, S.M.E. Sepasgozar, K. Zhang, S. Sepasgozar, F.A. Marroquin, Numerical analysis of the creep and shrinkage experienced in the Sydney Opera House and the rise of digital twin as future monitoring Technology, Buildings 137 (9) (2019).
[21] Y. Xia, Y.Q. Ni, P. Zhang, W.Y. Liao, J.M. Ko, Stress development of a supertall structure during construction: field monitoring and numerical analysis, Comput. Aided Civ. Infrastruct. Eng. 26 (2011) 542–559.
[22] C.M. Blanc, A.O. Sanchez, I.F. Navarro, Analytical characterisation of axial shortening due to creep of reinforced concrete columns in tall buildings, Eng. Struct. 228 (2021) 111584.
[23] H.N.P. Moragaspitiya, D.P. Thambiratnam, N.J. Perera, T.H.T. Chan, Development of a vibration-based method to update axial shortening of vertical load bearing elements in reinforced concrete buildings, Eng. Struct. 46 (2013) 49–61.
[24] F. Fan, H.J. Wang, X.D. Zhi, G. Huang, E.C. Zhu, H. Wang, Investigation of construction vertical deformation and pre-deformation control for three super high-rise buildings, Adv. Struct. Eng. 16 (11) (2013) 1885–1897.
[25] C.Q. Li, R.E. Melchers, Reliability analysis of creep and shrinkage effects, J. Struct. Eng. 118 (9) (1992) 2323–2337.
[26] Z.P. Bazant, J.C. Chern, Bayesian statistical prediction of concrete creep and shrinkage, ACI Journal 81 (29) (1985) 319–330.
[27] I.H. Yang, Prediction of time-dependent effects in concrete structures using early measurement data, Eng. Struct. 29 (2007) 2701–2710.
[28] I.H. Yang, Uncertainty and sensitivity analysis of time-dependent effects in concrete structures, Eng. Struct. 29 (2007) 1366–1374.
[29] S.S. Jin, S.L. Cha, H.J. Jung, Improvement of concrete creep prediction with probabilistic forecasting method under model uncertainty, Construct. Build. Mater. 184 (2018) 617–633.
[30] B.A. McElhoe, An assessment of the navigation and course corrections for a manned flyby of mars or venus, IEEE Trans. Aero. Electron. Syst. 2 (4) (1966) 613–623.
[31] M. Hoshiya, E. Saito, Structural identification by extended Kalman filter, J. Eng. Mech. 110 (12) (1984) 1757–1770.
[32] S.J. Julier, J.K. Uhlmann, Unscented filtering and nonlinear estimation, Proc. IEEE 92 (3) (2004) 401–422, 3.
[33] M. Wu, A.W. Smyth, Application of the unscented Kalman filter for real-time nonlinear structural system identification, Struct. Control Health Monit. 14 (7) (2007) 971–990.
[34] P.J.G. Teunissen, A. Khodabandeh, D. Psychas, A generalized Kalman filter with its precision in recursive form when the stochastic model is misspecified, J. Geodesy 95 (9) (2021) 108.
[35] B. Thomas, S. Chris, N. Doug, Toward a nonlinear ensemble filter for high-dimensional systems, J. Geophys. Res. Atmos. 108 (2003) 8775.
[36] P. Zarchan, H. Musoff, Fundamentals of Kalman Filtering: a Practical Approach, American Institute of Aeronautics and Astronautics, Incorporated, 2000.
[37] Q. Li, W.Z. Wu, R. Atiqur, Evolutionary deep learning with extended kalman filter for effective prediction modeling and efficient data assimilation, J. Comput. Civ. Eng. 33 (3) (2019) 04019014.
[38] X. Yu, D. Dan, Online frequency and amplitude tracking in structural vibrations under environment using APES spectrum postprocessing and Kalman filtering, Eng. Struct. 259 (2022) 114175.
[39] S.Y. Kim, C.H. Lee, Nondimensionalized Bouc–Wen model with structural degradation for Kalman filter–based real-time monitoring, Eng. Struct. 244 (2021) 112674.
[40] A.H. Abdullah, H. Achintya, Structural health assessment at a local level using minimum information, Eng. Struct. 88 (2015) 100–110.
[41] R. Lopez, J.P. Malarde, F. Royer, P. Gaspar, Improving Argos Doppler location using multiple-model Kalman filtering, IEEE Trans. Geosci. Rem. Sens. 52 (8) (2014) 4744–4755.
[42] Z. Yuan, G. Sun, X. Wu, et al., Research on vertical deformation and predeformation control of three-tower connected super high-rise structure during construction, Struct. Des. Tall Special Build. 31 (2022) e1913.
[43] H.S. Muller, H.K. Hilsdorf, Evaluation of the Time-dependent Behavior of Concrete, Summary Report on the Work of General Task Group 9, CEB Lausanne, Switzerland, 1990.
[44] D. E. Branson, M. L. Christiason. Time Dependent Concrete Properties Related to Design—Strength and Elastic Properties, Creep and Shrinkage. Creep, Shrinkage and Temperature Effects, SP-27, American Concrete Institute, Farmington Hills, MI, pp. 257-277..
[45] A. Aili, J.M. Torrenti, J.P. Sellin, On the long-term delayed strain of concrete structures, Cement Concr. Res. 165 (2023) 107086.
[46] C. Hajiyev, H.E. Soken, Robust adaptive unscented Kalman filter for attitude estimation of Pico satellites, Int. J. Adapt. Control Signal Process. 28 (2013) 107–120.
[47] B. Zheng, P. Fu, B. Li, X. Yuan, A Robust adaptive unscented kalman filter for nonlinear estimation with uncertain noise covariance, Sensors 18 (808) (2018).
[48] J. Zhou, S. Knelik, O. Loffeld, INS/GPS tightly-coupled integration using adaptive unscented particle filter, J. Navig. 63 (3) (2010) 491–511.
[49] D. Zou, C. Du, T. Liu, Time-dependent deformations of concrete columns under different construction load histories, Adv. Struct. Eng. 22 (8) (2019) 1845–1854.
[50] A.M. Neville, Recovery of creep and observations on the mechanism of creep of concrete, Applied Science Research 9 (1) (1960).
[51] M.H. Hubler, R. Wendner, Z.P. Bazant, Comprehensive database for concrete creep and shrinkage: analysis and recommendations for testing and recording, ACI Mater. J. 112 (4) (2015) 547–558.
[52] Z.P. Bazant, G.H. Li, Unbiased statistical comparison of creep and shrinkage prediction models, ACI Mater. J. 105 (6) (2008) 610–621.
[53] Z.P. Bazant, G.H. Li, Comprehensive database on concrete creep and shrinkage, ACI Journal 105 (6) (2008), 635-537.
[54] T.C.-107 Rilem, Guidelines for characterizing concrete creep and shrinkage in structural design codes or recommendations, Mater. Struct. 28 (1995) 52–55.
[55] H.S. Kim, S.H. Jeong, S.H. Shin, Column shortening analysis of tall buildings with lumped construction sequences, Struct. Des. Tall Special Build. 21 (10) (2012) 764–776.